How to cite: *Angew. Chem. Int. Ed.* **2024**, *63*, e202407909
doi.org/10.1002/anie.202407909

Zn-Ion Batteries

In-Situ Solid Electrolyte Interface via Dual Reaction Strategy for Highly Reversible Zinc Anode

Peiwen Xu, Mi Xu, Jie Zhang, Jiabin Zou, Yue Shi, Dan Luo, Dongdong Wang, Haozhen Dou, and Zhongwei Chen**

Abstract: In situ construction of solid electrolyte interfaces (SEI) is an effective strategy to enhance the reversibility of zinc (Zn) anodes. However, in situ SEI to afford high reversibility under high current density conditions ($\geq 20\,mA\,cm^{-2}$) is highly desired yet extremely challenging. Herein, we propose a dual reaction strategy of spontaneous electrostatic reaction and electrochemical decomposition for the in situ construction of SEI, which is composed of organic-rich upper layer and inorganic-rich inner layer. Particularly, in situ SEI performs as "growth binder" at small current density and "orientation regulator" at high current density, which significantly suppresses side reactions and dendrite growth. The in situ SEI affords the record-breaking reversibility of Zn anode under practical conditions, Zn//Zn symmetric cells can stably cycle for over 1300 h and 400 h at current densities of $50\,mA\,cm^{-2}$ and $100\,mA\,cm^{-2}$, respectively, showcasing an exceptional cumulative capacity of $67.5\,Ah\,cm^{-2}$. Furthermore, the practicality of this in situ SEI is verified in Zn//PANI pouch cells with high mass loading of $25.48\,mg\,cm^{-2}$. This work provides a universal strategy to design advanced SEI for practical Zn-ion batteries.

Introduction

Energy storage technologies are crucial for the integration of renewable energy sources and electrification across various sectors. Currently, lithium-ion batteries (LIBs) are the dominant battery technology for energy storage due to their high-energy density and long cycle life.[1–4] However, the increased economic costs and safety concerns limit their widespread utilization. Zinc-ion batteries (ZIBs) have emerged as one of the most promising energy storage technologies in the post-lithium-ion battery era, primarily due to the distinct advantages of high natural abundance of Zn, inherent safety of aqueous electrolytes, low oxidation-reduction potential of Zn anode (0.762 V vs. standard hydrogen electrode), and high theoretical capacity ($820\,mAh\,g^{-1}$).[5–9] Nevertheless, ZIBs encounter significant challenges, such as uncontrollable dendritic growth and notorious parasitic reactions of hydrogen evolution reaction (HER) and corrosion due to the absence of a stable solid-electrolyte interface (SEI). The unstable electrolyte-anode interface issues lead to the poor coulombic efficiency (CE) and short lifespan, thereby severely constraining their practical application.[10–12]

The construction of a stable SEI is paramount, serving to terminate the successive parasitic reactions between the Zn anode and the electrolyte, significantly improves the Zn plating/stripping efficiency and the cycle life of the Zn anode. The strategy for constructing SEI on the Zn anode surface can be broadly categorized into two types: in situ SEI,[13–15] or ex situ artificial SEI.[16–18] The in situ SEI construction strategy is attracting considerable attention because it is not only relatively economically feasible but also possesses robust self-healing properties, while synchronously suppressing HER and dendritic growth.[19] However, unlike organic electrolytes in LIBs, aqueous electrolytes in ZIBs are relatively difficult to form the stable SEI because they lack passivation components.[20] Currently, in situ SEI are mainly constructed by two strategies: the spontaneous electrochemical decomposition of electrolyte components or the spontaneous chemical reactions. Most in situ SEIs are formed through the electrochemical decomposition of anions and/or organic solvents in the electrolyte. The core of this approach involves the invasion of anions or organic solvents into the Zn^{2+} solvation shell by introduction of high concentrations salts and organic solvents, sacrificing the high safety and low cost of aqueous electrolytes and leading to the retarded interfacial reaction kinetics.[21–23] Another strategy is the use of certain unstable additives to help build in situ SEI in dilute electrolytes via spontaneous chemical reaction. Nevertheless, the resulting fragile and thick SEI layer is unable to support the long-term cycling of Zn stripping/plating, especially at high current density.[24–25] Consequently, relying solely on a single reaction strategy makes it difficult to achieve stable SEI operation at high current densities ($\geq 20\,mA\,cm^{-2}$) and high depth of discharge (DOD > 50 %).[26–27] To meet the requirements of an ideal SEI, a composite strategy is highly desirable to tailor the SEI component and structure. Be cleverly combining a

[*] P. Xu, M. Xu, J. Zhang, J. Zou, Y. Shi, D. Luo, D. Wang, H. Dou, Prof. Z. Chen
Power Battery & Systems Research Center
Dalian Institute of Chemical Physics, Chinese Academy of Sciences
Dalian, Liaoning, 116023, P. R. China.
E-mail: zwchen@dicp.ac.cn
haozhen@dicp.ac.cn
P. Xu, M. Xu, J. Zhang, J. Zou, Y. Shi, D. Luo, D. Wang, H. Dou
State Key Laboratory of Catalysis
Dalian Institute of Chemical Physics, Chinese Academy of Sciences
Dalian, Liaoning, 116023, P. R. China.

flexible organic phase and a rigid inorganic phase to form a composite structure, SEI can be made to combine fast ion transport and high tolerance to expansion/contraction stresses.[28–29] Simultaneously, the construction of a composite SEI facilitates synergistic interactions between the organic and inorganic phases to further enhance the stability of the SEI under harsh conditions.[30–31]

Herein, we propose a dual reaction strategy for in situ construction SEI, leveraging the synergism of spontaneous electrostatic reactions and electrochemical decomposition. This approach supports high reversibility of the Zn anode at a high current density of 100 mA cm^{-2} and a high DOD of 85.4 %. The ultrathin layered SEI is in situ constructed by introducing the functional additive (1-carboxymethyl-3-methylimidazolium chloride, CMIM) into low-concentration aqueous electrolytes. The spontaneous electrostatic reaction between CMIM and SO_4^{2-}/Zn^{2+} contributes to the organic-rich upper layer of SEI, while the electrochemical decomposition of SO_4^{2-} induces the inorganic-rich inner layer of SEI. Particularly, a detailed investigation of Zn^{2+} deposition mechanism reveals the in situ SEI performs as "growth binder" at small current density and "orientation regulator" at high current density. As expected, Zn//Cu asymmetric cells exhibit an ultralong cycle life of 2000 cycles with 99.5 % CE and Zn//Zn symmetric cells have achieved the record-breaking reversibility, which specifically sustain cycling stability for 1300 h at 50 mA cm^{-2} and 400 h at 100 mA cm^{-2}, thus showcasing an exceptional cumulative capacity (CC) of 67.5 Ah cm^{-2}. Especially for a high DOD (>85.4 %), long-term cycling stability for over 600 h is achieved at the areal capacity of 10 mAh cm^{-2}. Moreover, the practicability is also verified in Zn//PANI full and pouch cells with high-mass loading, demonstrating the superiority of in situ SEI. This work sheds light on the design of advanced SEI for highly reversible aqueous batteries under practical conditions.

Results and Discussion

CMIM has a unique molecular structure with a positively charged imidazole ring and a negatively charged –COO^- anion, allowing strong electrostatic interaction with both Zn^{2+} and SO_4^{2-} to form the organic-rich upper layer. Moreover, the imidazole ring binds strongly to SO_4^{2-}, which is enriched on the electrode surface and promotes the electrochemical decomposition of SO_4^{2-} to form a dense inorganic-rich inner layer. This dual-reaction strategy of synergistic spontaneous electrostatic reaction and electrochemical decomposition facilitates in situ construction of ultrathin layered SEI consisting of organic-rich organic upper layer and inorganic-rich inner layer (Figure 1a). Moreover, the addition of CMIM and in situ SEI foster additional benefits: (I) CMIM possesses hydrogen-bond acceptors and charged groups, which can disrupt the hydrogen-bond interactions among H_2O molecules and construct new interaction between CMIM and H_2O, thereby limiting H_2O activity and inhibiting HER reactions. (II) In situ SEI constructed by CMIM is conducive to the fast Zn^{2+} transfer/conduction, which guarantees the high reversibility of Zn anode at high current densities of 50 mA cm^{-2} and 100 mA cm^{-2}. As shown in Figure S1, all ZS-CMIM electrolytes maintain clear and transparent, and their ionic conductivities increase with increasing CMIM content. This further indicates that the positively charged imidazole ring and negatively charged –COO^- anion in CMIM effectively promote the interaction between electrolyte component ions, thereby improving ion conductivity (Figure S2).[32–34] Figure S3 shows the contact angles of 2 M $ZnSO_4$ electrolyte (shorted as BE) and ZS-CMIM electrolytes on the Zn anode. The addition of CMIM enhances the electrolyte wettability toward Zn anode, as verified by the decreased contact angle from 80.1° (BE) to 61.5° (ZS-CMIM$_{0.1}$).

The high reversibility of Zn anodes with ZS-CMIM electrolytes is evaluated by Zn//Zn symmetric cells and Zn//Cu asymmetric cells. All ZS-CMIM electrolytes demonstrate the significant improvements of cycling stability for Zn//Zn symmetric cells at current density of 0.5 mA cm^{-2} and areal capacity of 0.5 mAh cm^{-2}. Notably, the cell using the ZS-CMIM$_{0.1}$ electrolyte exhibits a prolonged lifespan of 6000 h while maintaining a steady overpotential of approximately 50 mV (Figure S4). In contrast, cells using BE have a higher polarization voltage and short circuit after approximately 50 h cycling. Therefore, the ZS-CMIM$_{0.1}$ electrolyte is chosen to evaluate other battery performances. Moreover, the CE of Zn stripping/plating in the BE and ZS-CMIM$_{0.1}$ electrolyte is measured by the Zn//Cu cells at 0.5 mA cm^{-2} and 0.5 mAh cm^{-2} (Figure 1b). ZS-CMIM$_{0.1}$ electrolyte achieves an average CE of 99.9 % and maintains stability for 2000 cycles. By contrast, the CE of Zn stripping/plating in the BE quickly fails at the 98th cycle. Remarkably, ZS-CMIM electrolytes significantly boost the cycling performance of Zn//Zn cells at high current densities and high DOD, demonstrating great potential for practical applications. Zn//Zn cell with ZS-CMIM$_{0.1}$ electrolyte shows the excellent cycling stability over 2500 h at current density of 5 mA cm^{-2} and 2 mAh cm^{-2} (Figure S5), while short circuit occurs in the ZS after less than 400 h. Particularly, Zn//Zn cells with ZS-CMIM$_{0.1}$ electrolyte deliver the stable operation for 2000 h at the current density of 20 mA cm^{-2} and 10 mAh cm^{-2} (Figure S6). Even under more demanding current density of 50 mA cm^{-2} (2.5 mAh cm^{-2}) and the highest current density of 100 mA cm^{-2} (5 mAh cm^{-2}), Zn//Zn cells with ZS-CMIM$_{0.1}$ electrolyte display the excellent stability for more than 1300 h and 400 h (Figure 1c, d and S7, S8). More importantly, ZS-CMIM$_{0.1}$ electrolyte can achieve a long cyclic lifespan of 600 h at high DOD of 85.4 % (Figure 1e). As shown in Figure 1f, the rate performance of Zn//Zn cells is investigated at different current densities. When the current density increases from 0.5 mA cm^{-2} to 100 mA cm^{-2}, the Zn//Zn cell with ZS-CMIM$_{0.1}$ electrolyte shows a steady plating/stripping curves, indicating the outstanding rate performance. As the current density reverts to 0.5 mA cm^{-2}, Zn//Zn cell continues to operate and returns to its initial voltage. In contrast, the cells with BE show large polarization voltages and experience a short circuit at 20 mA cm^{-2}. Furthermore, when benchmarked against presently reported electrolyte additives, the ZS-CMIM$_{0.1}$ electrolyte exhibits the remarkable

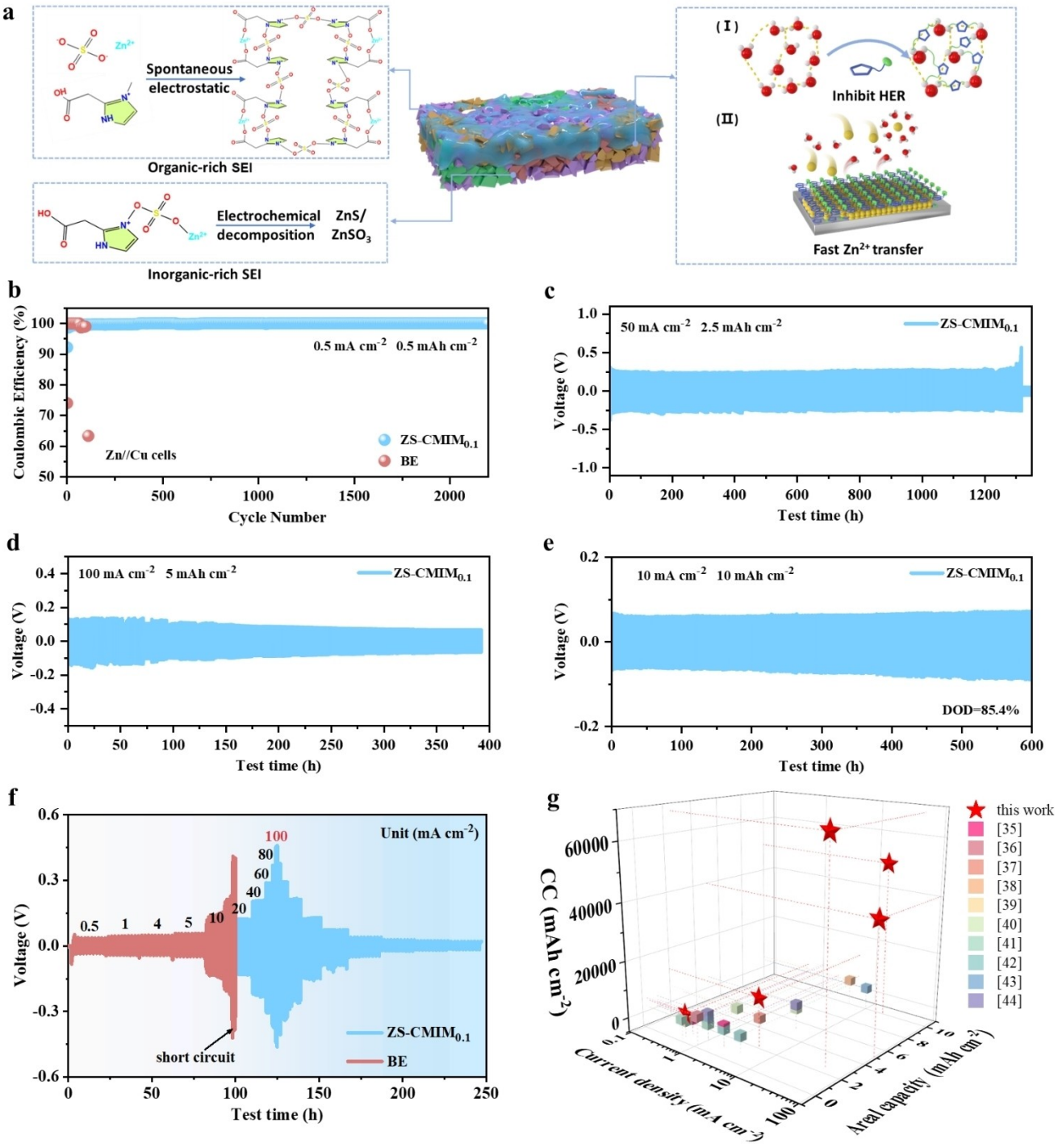

Figure 1. In situ construction of SEI via dual reaction strategy and the electrochemical performance of Zn anode. (a) Dual reaction strategy for in situ construction SEI. (b) CE of Zn//Cu half cells with BE and ZS-CMIM$_{0.1}$ electrolyte at 0.5 mA cm^{-2} and 0.5 mAh cm^{-2}. (c, d) Cycling performance of Zn//Zn symmetric cells with ZS-CMIM$_{0.1}$ electrolyte at 50 mA cm^{-2} (2.5 mAh cm^{-2}) and 100 mA cm^{-2} (5 mAh cm^{-2}). (e) Cycling performances of the high DOD (85.4%) Zn//Zn symmetric cells with ZS-CMIM$_{0.1}$ electrolyte at 10 mA cm^{-2} and 10 mAh cm^{-2}. (f) Rate performance of Zn//Zn symmetric cells assembled with BE and ZS-CMIM$_{0.1}$ electrolyte. (g) Comparison of cycling performance of Zn//Zn symmetric cells between this work and other reported works.

cycling efficiency under exceptional current densities. As illustrated in Figure 1g, the ZS-CMIM$_{0.1}$ electrolyte achieves a CC of 67.5 Ah cm^{-2}, marking the highest record in electrolyte engineering thus far.[35–44] Additionally, the high DOD cycling performance of the ZS-CMIM$_{0.1}$ electrolyte outperforms that of recently reported electrolyte additives (Table S2).

The liquid structure of ZS-CMIM electrolyte is investigated using Fourier transform infrared (FTIR), nuclear magnetic resonance (NMR), and Raman spectra. Figure 2a and S9 illustrate the O–H stretching vibration of H_2O within the range of 2500–4000 cm^{-1}. Upon adding CMIM, the O–H stretching vibration mode shows blueshift. Three discernible peaks corresponding to strong hydrogen bonds (HB), mediate HB, and weak HB have been identified.[45–46] The weak HB dramatically increase with increasing CMIM content, suggesting that the addition of the introduction of CMIM effectively alters the initial HB network in BE, consequently weakening the HB among H_2O molecules. The reconstructed HB network is further supported by ^1H NMR spectra. The chemical shift of H_2O exhibits a gradual downward-shift behavior with increasing CMIM content, further confirming the enhanced HB interaction between H_2O and CMIM (Figure 2b).[47] As shown in the Raman spectra (Figure 2c), there are no significant variations in the stretching vibration of SO_4^{2-} in the different ZS-CMIM electrolytes, which illustrates that trace amounts of CMIM molecules have a limited effect on the Zn^{2+} solvated sheath. However, the stretching vibration peak of H_2O shifts toward a higher wavenumber as the CMIM content increases. This indicates an amplified interaction between the CMIM additive and H_2O molecules, inhibiting the activity of H_2O molecules. To further elucidate the interaction behavior among H_2O, Zn^{2+} and CMIM additive, density functional theory (DFT) calculations are performed (Figure S10). The calculated CMIM−H_2O binding energy is found to be −19.26 kcal/mol, exceeding that of the H_2O–H_2O (−6.30 kcal/mol). This result suggests that CMIM molecules tend to capture H_2O via strong HB interactions, leading to the reorganization of the three-dimensional HB network of electrolyte.[48]

Gibbs free energies (ΔG) are then employed to quantify the thermodynamics energy barrier of HER on the Zn anode (Figure. 2d).[49] The Zn anode in the ZS-CMIM electrolyte exhibits a higher energy barrier (ΔG = −1.92 eV) than that of BE (ΔG = −1.61 eV), suggesting an increased ability of ZS-CMIM electrolyte to impede the HER. More-

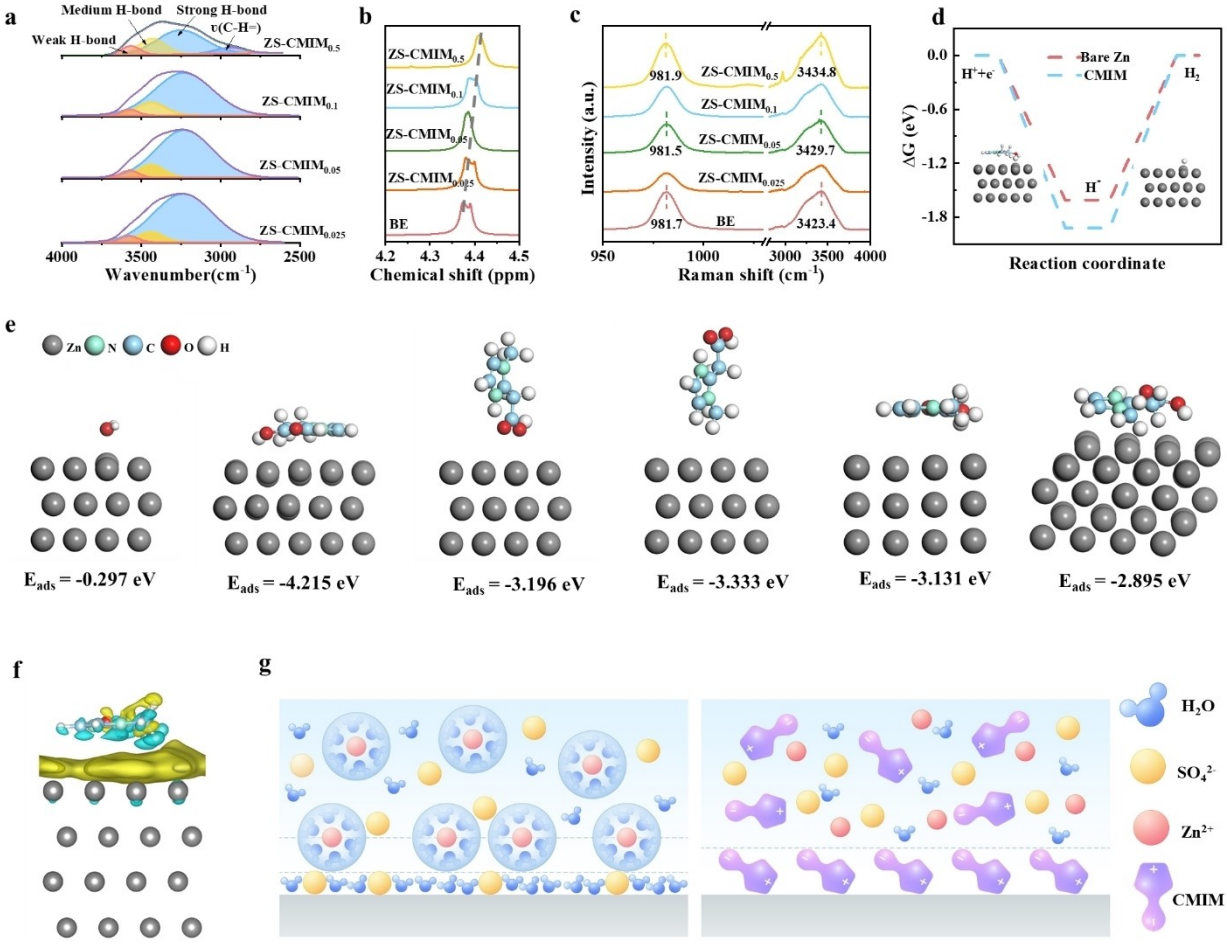

Figure 2. Spectroscopy analysis and theoretical calculation of electrolyte and EDL structures. (a) The fitted FTIR spectra of O–H stretching band of water in BE and ZS-CMIM electrolytes. (b) ^1H NMR of BE and ZS-CMIM electrolytes. (c) Raman spectra of BE and ZS-CMIM electrolytes. (d) Energy barrier of HER in BE and ZS-CMIM electrolytes. (e) Adsorption modes of H_2O, CMIM molecules on Zn (002) surface under different molecular arrangements, and parallelly placed CMIM molecules on (101)/ (100) Zn surface and corresponding adsorption energy. Color code: red O, white H, sky blue C, aqua N and gray substrate Zn anode. (f) Charge density difference of Zn (002) with parallelly placed CMIM adsorption. (g) Schematic descriptions of EDL structure before and after introducing CMIM.

over, linear sweep voltammetry (LSV) is conducted to assess the HER and oxygen evolution reaction (OER). In the ZS-$CMIM_{0.1}$ electrolyte, the onset potential of HER reduces from −0.13 V to −0.28 V vs Zn/Zn^{2+}, indicating the successful inhibition of the HER. Meanwhile, the increased OER overpotential further substantiates the beneficial impact of CMIM additive on inhibiting H_2O decomposition (Figure S11). Notably, ZS-$CMIM_{0.1}$ electrolytes can suppress the self-corrosion of Zn anode, as validated by the soaking of polished Zn anodes in BE and ZS-$CMIM_{0.1}$ electrolyte for 7 days. Scanning electron microscopy (SEM) images (Figure S12) demonstrate that the surface of Zn anode soaked in the BE is covered with loosely stacked hexagonal flakes, whereas no significant change is visible on the surface of Zn anode soaked in the CMIM electrolyte. The X-ray diffraction (XRD) pattern of Zn anode in the BE shows strong characteristic peaks corresponding to $Zn_4SO_4(OH)_6 \cdot xH_2O$ by-product. In contrast, the peak of by-product is much weaker in the ZS-$CMIM_{0.1}$, suggesting that ZS-$CMIM_{0.1}$ electrolytes can effectively inhibit the occurrence of side reactions (Figure S13).

The structure and chemistry of electrolyte-electrode interface is investigated to gain insights into the mechanism of CMIM for performance enhancement. The adsorption behavior of CMIM and corresponding adsorption energy of CMIM on the Zn anode are analyzed using DFT calculations (Figure 2e). The adsorption energy of parallelly placed CMIM (−4.215 eV) towards (002) crystal plane of Zn anode is notably higher than the values obtained for H_2O (−0.297 eV), vertically placed CMIM with carboxylate-anionic adsorption site (−3.196 eV), vertically placed CMIM with imidazole-cationic adsorption site (−3.333 eV), indicating that CMIM molecules are preferentially adsorbed on the Zn surface in a parallel orientation. Comparing the adsorption energy of CMIM on various Zn planes reveals that the adsorption energy of CMIM to the (002) plane is lower than that of the (100) plane (−3.131 eV) and the (101) plane (−2.895 eV). This illustrates more (002) crystal planes are exposed due to preferential adsorption of CMIM.[50] Similarly, the differential charge density distribution reveals the strong chemical adsorption of CMIM towards Zn anode, where the obvious electron transfer occurs from CMIM to Zn anode(Figure 2f and S14). Consequently, a localized CMIM-rich and H_2O-poor electric double layer (EDL) is spontaneously formed due to the preferential chemisorption on the Zn anode (Figure 2g), as evidenced by the following molecule dynamics (MD) simulations.

EDL plays a crucial role in the formation of the SEI, where the components preferentially adsorbed in the electrolyte exhibit a strong correlation with the SEI chemistry and structure.[51–52] As highlighted by MD simulations, CMIM molecules significantly alter the structure of the EDL. Typically, due to the large energy required for dehydration, hydrated Zn^{2+} cannot directly approach the Zn anode but primarily interact with H_2O dipoles. As a result, H_2O-rich EDL structure form near the Zn anode surface, enhancing side reactions (Figure S15–S16). After the addition of CMIM, due to the strong chemisorption, the free CMIM molecules can break through the inner Helmholtz plane and get closer to the Zn anode than the H_2O molecules (Figure 3a and S17). Due to the unique molecular conformation of CMIM, which contains both positive and negative charges, these molecules preferentially anchor to the negatively charged electrode surface by strong electrostatic adsorption, forming a CMIM molecule-rich and H_2O-poor EDL. In addition, normalized density profiles are shown in Figure 3b and S18 for quantitative interpretation. Regardless of whether the Zn anode surface is zero or negatively charged, CMIM molecules are adsorbed and enriched on the electrode surface, while the spatial density of H_2O molecules at the interface decreases dramatically, resulting in the formation of H_2O-poor EDLs, which improves cathodic stability.

The SEI formation in the ZS-$CMIM_{0.1}$ electrolytes is studied by X-ray photoelectron spectroscopy (XPS), time-of-flight-secondary ion mass spectrometry (TOF-SIMS) and focused ion beam-SEM (FIB-SEM). The surface composition of the Zn anode after 30 cycles is investigated using TOF-SIMS. A three-dimensional view of the distribution of the Zn, S and O elements (Figure 3c) indicates that for the Zn anode cycled in BE, these species are uniformly distributed within the detection depth. However, in the ZS-$CMIM_{0.1}$ electrolyte, these elements are present only on the surface of the Zn anodes, indicating the formation of a dense SEI layer (Figure S19 and S20), preventing H_2O penetration and reducing Zn corrosion. In-depth interphase analysis using FIB confirms that ZS-$CMIM_{0.1}$ electrolyte has the advantage of forming a uniform, light-colored SEI layer during cycling (Figure S21). The Zn deposition exhibits a very dense structure without any obvious defects. In contrast, in the BE, the cycled Zn anode presents a porous structure, leading to rapid volume expansion and uncontrolled interfacial side reactions. Figure S22 shows the in situ EIS curves of Zn//Zn-symmetric cells using BE and ZS-$CMIM_{0.1}$ electrolytes during different cycles, concluding that the stable interface has been obtained in ZS-CMIM0.1 electrolytes during initial-activation cycles, while the interface impedance of the Zn anode in BE electrolyte continues to increase due to the endlessly side reactions.[53]

To gain a deeper understanding of the overall structure of the SEI, the compositional distribution in the SEI is analyzed in detail using the XPS with Ar^+ sputtering depth profile (Figure 3d and S23). On the surface of SEI in ZS-$CMIM_{0.1}$ electrolyte, N 1s signal exists as Zn–N at 399.4 eV is attributed to the bonding of the imidazole ring with Zn^{2+}.[54] Notably, the O 1s spectra exhibit significant differences between the two electrolyte systems. In the BE, O 1s spectra has two major components corresponding to SO_4^{2-} and the $Zn(OH)_2$, which still remains with increasing sputtering time. This indicates that in BE, due to the lack of SEI, the side reactions continuously corrode the Zn anode. (Figure S24). Conversely, in the ZS-$CMIM_{0.1}$ electrolyte, the O 1s spectra of the surface of Zn anode shows only one component: $Zn(RCOO)_2$, representing the organic component forming the SEI. After further sputtering to a depth of 3 min, the organic component disappears, replaced by inorganic components represented by ZnO and $ZnCO_3$ (Figure S25). The formation of a layered SEI with an

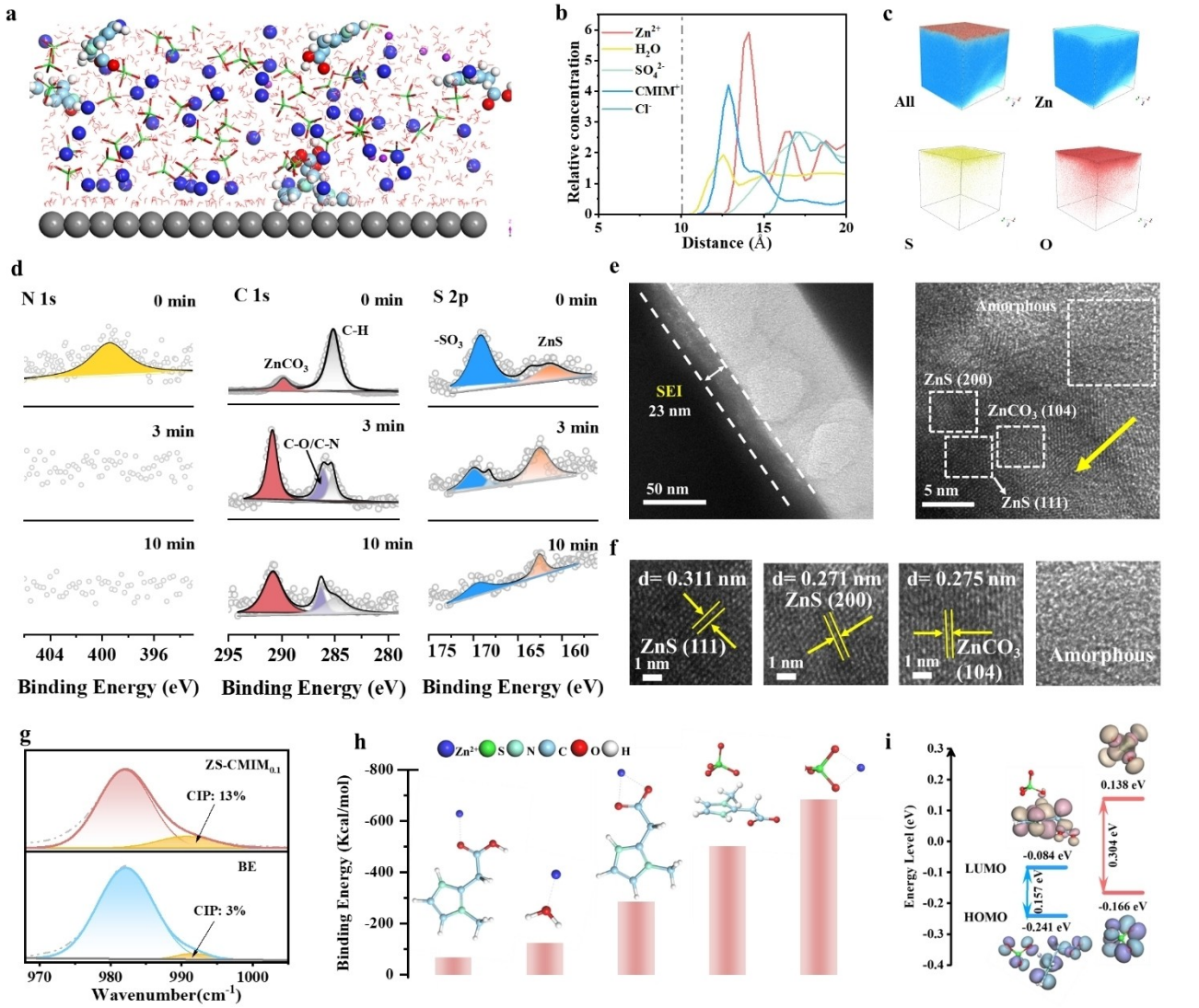

Figure 3. Characterization and theoretical simulation of EDL and SEI structure. (a) The snapshot of EDL structure for Zn anode interface in ZS-$CMIM_{0.1}$ electrolyte at negative charged. (b) Normalized density profiles of different ingredients on Zn anode surfaces in ZS-$CMIM_{0.1}$ electrolyte at negative charged. (c) TOF-SIMS three-dimensional render images of Zn anode surface tested in ZS-$CMIM_{0.1}$ electrolyte for 30 cycles. (d) The XPS depth spectra for S 2p, N 1s and C 1s of Zn anode tested in ZS-$CMIM_{0.1}$ electrolyte for 30 cycles. (e) Transmission electron microscopy characterization (TEM) for SEI morphology formed in ZS-$CMIM_{0.1}$ electrolyte. (f) High-resolution TEM (HRTEM) images of amorphous organic component, $ZnCO_3$ and ZnS within SEI formed in ZS-$CMIM_{0.1}$ electrolyte. (g) ATR-SEIRAS spectra of the ν-SO_4^{2-} bond for BE and ZS-$CMIM_{0.1}$ electrolyte. (h) DFT calculations of binding energies between any two ingredients in ZS-$CMIM_{0.1}$ electrolytes. (i) LUMO, HUMO iso-surfaces of CMIM-$SO4^{2-}$ (left) and free $SO4^{2-}$ (right).

organic upper layer and an inorganic inner layer is confirmed. This layered SEI is further confirmed in the C 1s and S 2p spectra primarily. The C 1s spectra consist of three main species: $ZnCO_3$ (~290.0 eV), C–N/C–O (286.2 eV), and C–C/C–H (285.1 eV). As the sputtering time increases, the intensity levels of the inorganic component represented by $ZnCO_3$ and that of C–O/C–N/C–H represented by the intensity levels of the organic components are inversely related. In addition, $-SO_3$ species (169.9 eV) and ZnS (162.3 eV), representing inorganic components, are also confirmed in the S 2p spectra.[55] Consequently, the SEI formed in the ZS-$CMIM_{0.1}$ electrolyte exhibits an ultrathin layered SEI with an outer organic-rich layer and an inner inorganic-rich layer. To verify the stability of this layered SEI, XPS analysis is also performed on the surface of the Zn anode after long cycling. The results showed that the organic–inorganic layered SEI structure still existed stably on the surface of the Zn anode after long cycling. (Figure S26–27)

To confirm the presence of the SEI, Transmission Electron Microscopy (TEM) is utilized to image the zinc surface after cycling. An even and intact interphase layer, with a thickness of 23 nm, is defined as an ultrathin SEI layer on the Zn anode surface (Figure 3e and S28). The microstructure of the SEI components is thoroughly analyzed by High-Resolution TEM (HRTEM) with further

magnification (Figure 3f). It's notable that along the yellow arrows from the outer region of the SEI to the inner side of the Zn anode, the amorphous organic component gradually decreases, and well-crystallized inorganic grains are mainly exposed in the inner region of the SEI. The inorganic components identified by lattice spacing are predominantly ZnS and $ZnCO_3$. To confirm the formation mechanism of this ultra-thin layered SEI, spectral analysis is employed to characterize the surface chemistry of the interface between the Zn anode and electrolyte. Through the ATR-SIRAS spectroscopy, it's observed changes in the ν-SO_4^{2-} bond at the electrode interface in the range of 981–985 cm^{-1}, which can be attributed to the presence of solvent-shared ion pairs (SSIPs) and contact ion pairs (CIPs) (Figure 3g). In the ZS-$CMIM_{0.1}$ system, the proportion of CIPs increases from 3 % to 13 %, confirming the strong electrostatic interactions between CMIM and SO_4^{2-} at the interface, which promotes the entry of SO_4^{2-} into the inner solvation sheath and thus facilitates the SO_4^{2-} reduction process.[25,56] Similarly, the ATR-FTIR spectra of Zn anode soaked in ZS-$CMIM_{0.1}$ electrolyte shows –C–N– and –N–H– functional group absorption peaks (Figure S29).[54] Compared with the CMIM standard sample, the change of peak shape and the shift of position indicate the spontaneous electrostatic reaction between CMIM and Zn^{2+}/SO_4^{2-}.

DFT calculations are employed to explore the electrostatic interactions between CMIM, Zn^{2+} and SO_4^{2-}. The results show that the interaction energy between Zn^{2+} and SO_4^{2-}, as well as CMIM, significantly exceeds that between Zn^{2+} and H_2O (Figure 3h). CMIM couples more readily subjected to spontaneous electrostatic reaction with Zn^{2+} and SO_4^{2-}, facilitating the formation of an organic-rich SEI layer at the electrode-electrolyte interface (Figure S30). This organic-rich SEI layer exhibits high flexibility and adheres tightly to the Zn anode surface to prevent peeling. It also forms a fast Zn^{2+} conduction channel, facilitated by the strong interaction between CMIM and Zn^{2+}. This feature is particularly important at high current densities and contributes to the overall stability of the battery. Importantly, the imidazole ring of CMIM has a strong adsorption capacity for SO_4^{2-} (−500.61 kcal/mol), which can trap SO_4^{2-} on the surface of the Zn anode, probably contributing to the electrochemical decomposition of SO_4^{2-} and thus forming the inorganic-rich SEI layer.

Molecular orbital level calculations are also conducted to further investigate the SEI formation mechanism of dual reaction strategy. As illustrated in Figure 3i, which compares the reduction ability of SO_4^{2-} bound to CMIM and free SO_4^{2-} in the electrolyte. The results showed that SO_4^{2-} bound to CMIM has a lower lowest unoccupied molecular orbital (LUMO) energy level, indicating that it is more susceptible to reduction and the formation of low-valence sulfur products such as ZnS.[57] And the CMIM molecule exhibits a higher position of the highest occupied molecular orbital (HOMO) compared to that of H_2O (−7.81 eV vs. −6.84 eV), which easily transfer electron to Zn^{2+} via electrostatic interaction for in situ SEI construction(Figure S31).[58] In addition, the LUMO energy level of CMIM (−1.87 eV) is much lower than that of H_2O (0.64 eV), which facilitates its preferential formation of SEI by coordinating SO_4^{2-} before Zn deposition.

CMIM is enriched on the surface of Zn anode, contributing to the spontaneous formation of the organic component of the SEI during Zn stripping/plating process, whereas SO_4^{2-} trapping by the imidazole ring preferentially constructs the ZnS inorganic component by electrochemical decomposition. Generally, hybrid SEI containing both organic and inorganic species may be more expected, which generally inherits the advantages of organic and inorganic species at the same time. The organic outer layer inhibits water penetration into the Zn surface and prevents layer fracture, while the inorganic inner layer promotes Zn^{2+} diffusion and inhibits the vertical growth of dendrites.

The Zn deposition behavior and the morphology evolution of Zn anode in BE and ZS-$CMIM_{0.1}$ electrolytes are studied. DFT calculations are employed to determine the migration energies of Zn^{2+} on the Zn anode surface. The migration energies of Zn^{2+} remain low and do not exceed 0.136 eV in the BE (Figure S32). Consequently, Zn^{2+} ions exhibit a strong thermodynamic tendency to proceed two-dimensional (2D) diffusion across the surface, ultimately leading to dendrite formation. However, with the introduction of CMIM molecules, the migration energy barriers for Zn^{2+} increase to 0.857 eV, significantly hindering the 2D diffusion (Figure 4a). SEM is performed to observe Zn^{2+} nucleation at different plating times. In the BE, the initial nuclei display a larger volume, irregular shape, and sparse distribution. Additionally, as highlighted by high-resolution SEM images, the deposited metallic Zn exhibits micrometer-sized blocky crystals with predominantly (101) directional vertical texture (Figure 4b and S33). In contrast, the nuclei in the ZS-$CMIM_{0.1}$ electrolyte are much smaller and densely distributed, readily forming dense deposition as nuclei merge. The nucleation mechanism is examined using cyclic voltammetry (CV) and chronoamperometry (CA) measurements. In the BE, the current intensity continued to increase steadily throughout the process. This pattern indicates a prolonged duration of the two-dimensional (2D) diffusion process, where Zn^{2+} ions tend to aggregate and grow into dendrites to minimize surface energy and exposed area. Contrastingly, in the ZS-$CMIM_{0.1}$ electrolyte, the diffusion of Zn^{2+} ions exhibit a three-dimensional dominance owing to the robust ligand interactions between Zn^{2+} and CMIM, enhancing charge transfer kinetics (Figure 4c). Consequently, Zn^{2+} ions in this environment are more susceptible to reduction and nucleation in the active site, thereby promoting uniform and dense Zn deposition. The superior charge transfer in the ZS-$CMIM_{0.1}$ electrolyte is corroborated by CV curves. As illustrated in Figure S34, the onset potential for Zn^{2+} nucleation in ZS-$CMIM_{0.1}$ is notably higher than that in the BE, suggesting that the ZS-$CMIM_{0.1}$ electrolyte is more conducive to the rapid transfer and nucleation of Zn^{2+}. These findings indicate that the ultrathin layered SEI can modulate the orientation of Zn deposition and promote dendrite-free behavior.

The uniform Zn nucleation and constrained 2D diffusion contribute to the even deposition with high CE, as

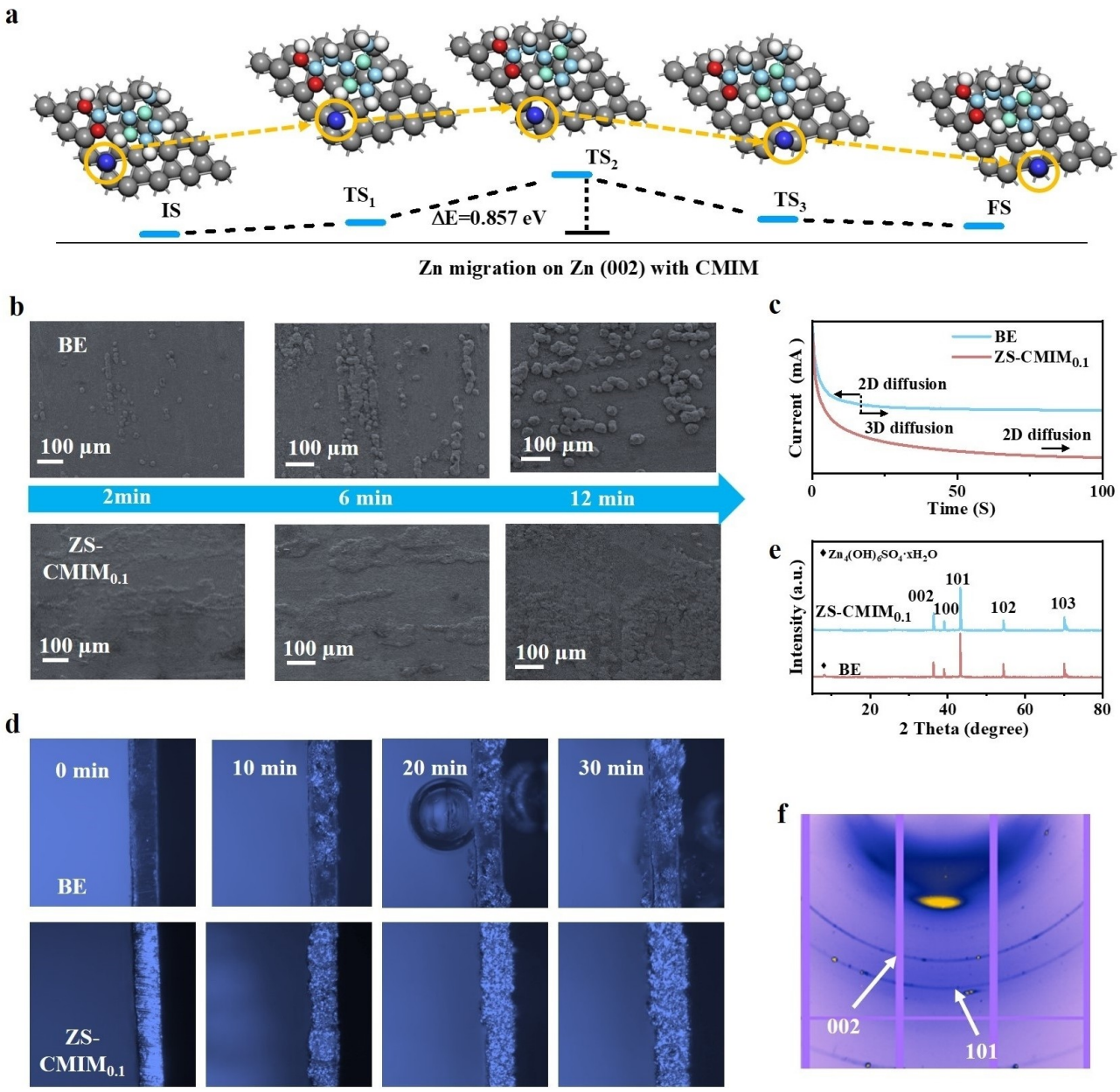

Figure 4. Characterization for electrodeposition morphology of Zn anode. (a) Zn^{2+} migration positions and migration energy on Zn (002) in ZS-$CMIM_{0.1}$ electrolyte. (b) SEM images of Zn nucleation under different deposition time in BE and ZS-$CMIM_{0.1}$ electrolytes at 1 mA cm^{-2}. (c) Chrono-amperometry (CA) curves of Zn anode in BE and ZS-$CMIM_{0.1}$ electrolytes, respectively. (d) In situ optical microscopy images of Zn electrode during Zn plating/stripping in BE and ZS-$CMIM_{0.1}$ electrolyte, respectively. (e) XRD patterns of Zn anode in BE and ZS-$CMIM_{0.1}$ electrolytes at 100th cycles, respectively. (f) 2D GIXRD pattern of deposited Zn in ZS-$CMIM_{0.1}$ electrolytes at 100th cycles.

evidenced by the in situ optical microscopy characterization of Zn deposition at 1 mA cm^{-2} (Figure 4d). In the BE, Zn anode surface is overgrown with the randomly-distributed protrusions after 10 min. Due to the "tip effect," these protrusions trigger self-amplifying growth with electrodeposition, gradually evolving into large isolated Zn dendrites, accompanied by bubble generation. In contrast, in the ZS-$CMIM_{0.1}$ electrolyte, the Zn anode maintains a flat surface without dendrites during the plating process. Therefore, the in situ SEI regulates the Zn nucleation and Zn^{2+} diffusion, thus ensuring the uniform Zn deposition.

To further investigate the in situ SEI on Zn reversibility, the morphology evolution of Zn anode after the 10th, 30th, and 100th cycles are compared by SEM images. In the BE, Zn anode presents a rough surface with a large number of Zn dendrites and glass fibers. In contrast, after cycling for 100 cycles in the ZS-$CMIM_{0.1}$ electrolyte, the Zn anode shows a smooth surface (Figure S35). Meanwhile, XRD pattern of the Zn anode after 100 cycles in the ZS-$CMIM_{0.1}$ electrolyte does not reveal any by-products originating from irreversible corrosion (Figure 4e). More importantly, an enhancement of the (002) crystal plane is observed. In

contrast, distinct characteristic peaks of $Zn_4SO_4(OH)_6{\cdot}xH_2O$ are visible in the XRD pattern of the Zn anode cycled in the BE. Similarly, two-dimensional grazing-incidence X-ray diffraction (2D-GIXRD) patterns of Zn anode further reveal the enhanced (002) crystal plane orientation in the ZS-$CMIM_{0.1}$ electrolyte(Figure 4f and S36).These findings reveal that the in situ SEI effectively achieves the dendrite-free Zn anode and manipulates the crystal orientation.[59]

The working mechanism of in situ SEI on the modulation of Zn deposition behavior under different current densities is investigated through detailed morphology analysis of Zn deposition in the BE and ZS-$CMIM_{0.1}$ electrolytes, where a consistent deposition capacity of 10 mAh cm^{-2} is maintained in the experiments (Figure 5a–5f and S37). The Zn deposition involves two main phases, nucleation and growth, and is controlled by various factors, such as crystallographic thermodynamics, kinetics, and Zn^{2+} diffusion.[60] At low current densities (0.5 mA cm^{-2}), Zn deposition is controlled by surface energy, and the morphology coincides with the crystal thermodynamics of the (101) plane. In the BE, a deposition layer is formed by the accumulation of a large number of large-sized spherical Zn dendrites with discrete distribution. However, in the ZS-$CMIM_{0.1}$ electrolyte, a large, dense, and flat Zn deposition layer is formed, containing many connected grains, where thickness of deposition layer (142 μm) is much thinner than that in the BE (288 μm). This indicates that the in situ SEI promotes ionic diffusion and guides Zn deposition at low current densities, which acts as "nucleation binders," connecting Zn deposition grains, significantly increasing the quantity of Zn nucleation and the compaction of Zn deposition. When the current density increases to 10 mA cm^{-2}, the Zn deposition behavior alters, with the process kinetically controlled, activating high-index crystal surfaces. Zn electrode deposition shifts morphologically from nanosheets to bulk crystals. In the BE, the uneven and thick deposition layer (29 μm) adopts a hillock-like morphology, comprising disordered stacked hexagonal plates. Conversely, ZS-$CMIM_{0.1}$ electrolyte delivers a uniform and dense Zn deposition layer with an approximate uniform

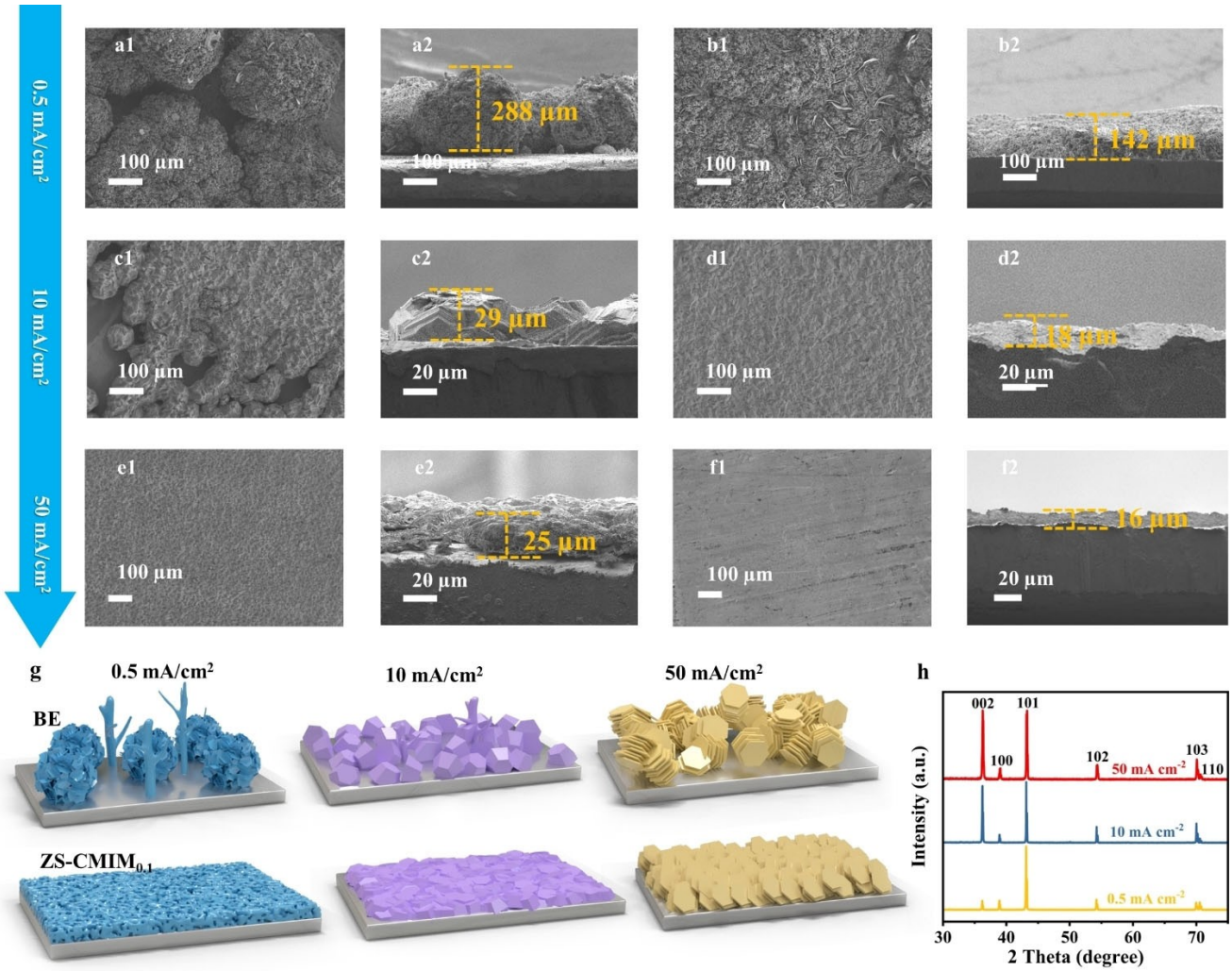

Figure 5. Structure evolution of Zn anodes at different current densities. (a) SEM images of the Zn metal deposited at different current densities (0.5–50 mA cm^{-2}) in the BE (a, c, e) and ZS-$CMIM_{0.1}$ electrolyte (b, d, f). (g) Schematic illustration of deposition mechanism in BE and ZS-$CMIM_{0.1}$ electrolyte. (h) XRD patterns of the deposited Zn at different current densities (0.5–50 mA cm^{-2}) in ZS-$CMIM_{0.1}$ electrolyte.

thickness of 18 μm, comprising horizontally arranged hexagonal crystal blocks and demonstrating a robust (002) texture.

Under higher current density conditions (50 mA cm^{-2}), in situ SEI serve as "orientation regulator" for Zn deposition. The ZS-CMIM$_{0.1}$ electrolyte affords the orderly and fine Zn deposition composed of large-sized lamellar Zn plates with single crystal orientation. The regular morphology of Zn deposition results in a reduced electrolyte-accessible surface, minimizing dendrite-growth and facilitating Zn anode reversibility. Conversely, in the BE, Zn deposition manifest as a porous and mess layer, where evident cracks, uneven plating heights, and poor morphological uniformity exacerbate side reactions. The rapidly depleted Zn ions within the electrolyte and insufficient Zn^{2+} diffusion at high current density result in a loosely packed and porous Zn deposition, which is susceptible to peel off from Zn anode.[61] The in situ SEI effectively achieves uniform electrochemical Zn deposition under high current conditions.

To assess the practical applicability of the CMIM additive, PANI cathode is coupled with Zn metal to construct full ZIBs. CV curves with the ZS-CMIM$_{0.1}$ electrolyte show the identical redox behavior compared to the BE, implying that the cathode reaction mechanism remains unchanged (Figure 6a).[62] Subsequently, the long-term cycle performance is evaluated at 3 A g^{-1}. Figure 6b shows that the Zn//PANI cell operating in BE displays rapid capacity degradation after 3000 cycles, with a relatively low CE and a retention rate of only 28 %. This degradation is attributed to

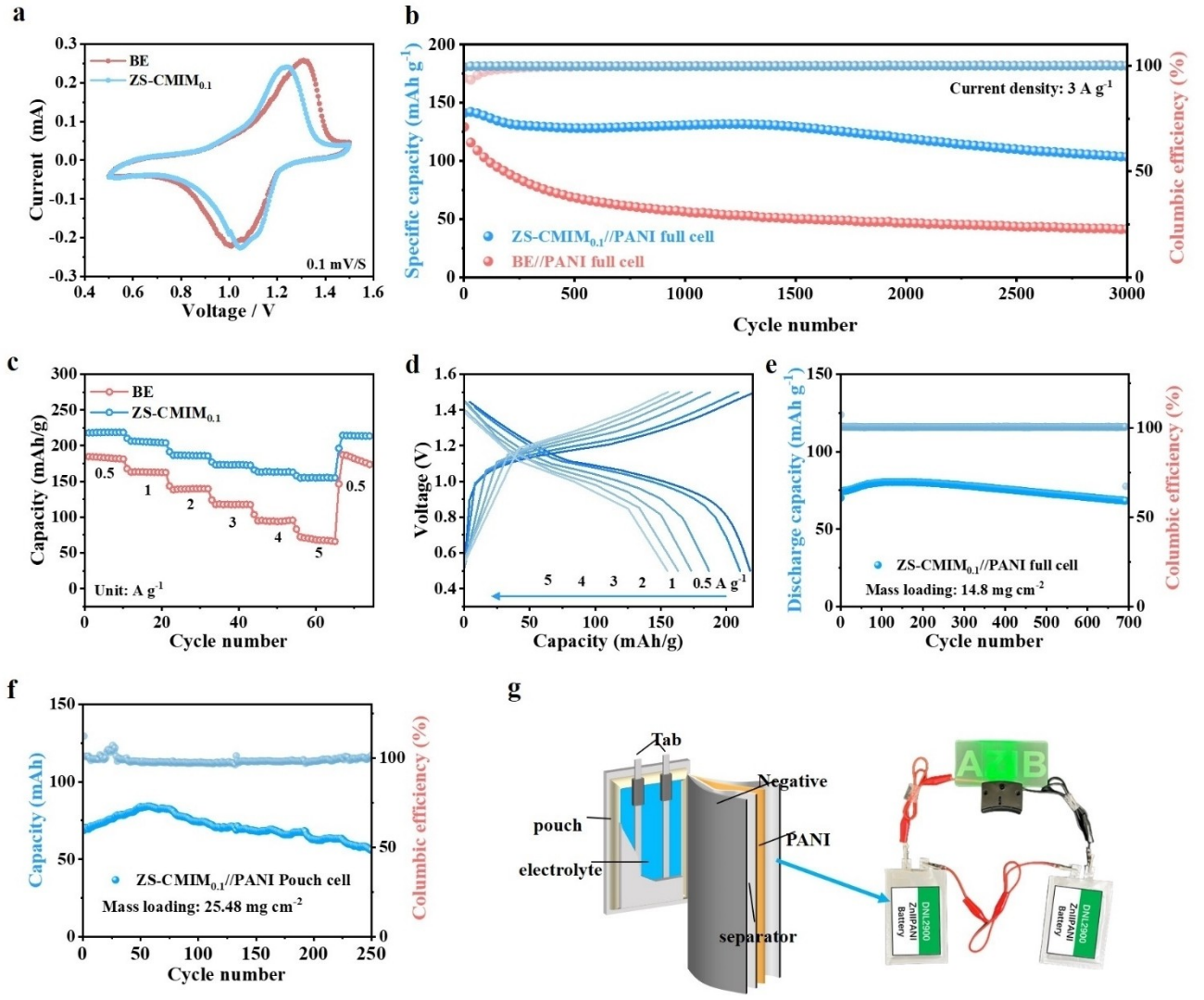

Figure 6. Electrochemical performance of Zn//PANI batteries using BE and ZS-CMIM$_{0.1}$ electrolytes. (a) Cyclic voltammetry (CV) curves for Zn//PANI batteries using BE and ZS-CMIM$_{0.1}$ electrolyte. (b) Galvanostatic cycling performance and CE of Zn//PANI batteries using BE and ZS-CMIM$_{0.1}$ electrolyte. (c) Rate performance of Zn//PANI batteries using ZS-CMIM$_{0.1}$ electrolyte. (d) Charge-discharge profiles at different current densities using ZS-CMIM$_{0.1}$ electrolytes. (e) Cycling performance and CE of Zn//PANI batteries using ZS-CMIM$_{0.1}$ electrolyte with high mass loading 14.8 mg cm^{-2}. (f) Cycling performance and CE of Zn//PANI pouch cell using ZS-CMIM$_{0.1}$ electrolyte with high mass loading 25.48 mg cm^{-2}. (g) A digital photograph showing LEDs powered by Zn//PANI pouch cells in series operated in ZS-CMIM$_{0.1}$ electrolytes.

dendrite formation and increased side reactions. Conversely, the ZS-$CMIM_{0.1}$ battery demonstrates superior long-term cycling stability after 3000 cycles, maintaining a CE above 99 %. Furthermore, the Zn//PANI cell with ZS-$CMIM_{0.1}$ electrolyte exhibits a fast capacitive-dominated charge storage mechanism and superior rate performance. At currents of 0.1, 0.5, 1.0, 2.0, 5.0, and 10.0 $A g^{-1}$, it achieves specific capacities of 244.8, 231.7, 212.5, 199.3, 185.3, and 168.8 $mAh g^{-1}$, respectively (Figure 6c, 6d, and Figure S39). All these values surpass the discharge-specific capacity of the ZS electrolyte at the corresponding current densities, demonstrating the crucial role of CMIM in interfacial stability and reaction kinetics. Importantly, when the current density reverts to 0.5 $A g^{-1}$, the full cell using ZS-$CMIM_{0.1}$ electrolyte retains a satisfactory capacity, strongly indicating that CMIM additive suppress dendrite growth and alleviate H_2O-induced parasitic reactions. More impressively, the Zn//PANI full cells with ZS-$CMIM_{0.1}$ electrolyte are able to cycle stably for more than 700 cycles and maintain 97.5 % reversible capacity, even at a high active mass–loaded cathode of 14.8 $mg cm^{-2}$ (Figure 6e). Pouch cells of Zn// PANI are assembled to extend the assessment of the ZS-$CMIM_{0.1}$ application potential. As shown in Figure 6f, pouch cells utilizing the ZS-$CMIM_{0.1}$ electrolyte exhibit an impressive initial capacity of 68 mAh and sustain a lifespan of 250 cycles. Furthermore, when two pouch cells are connected in series, they successfully power an LED bulb (3 eV), providing tangible evidence of the practical application potential of the designed Zn batteries (Figure 6g).

Conclusion

We present a dual-reaction strategy for in situ SEI construction that aims to manipulate the distinctive molecular structure of CMIM additives to form an ultrathin layered SEI consisting of an organic-rich top layer and an inorganic-rich inner layer through the synergistic effect of spontaneous electrostatic reaction and electrolyte electrochemical decomposition. A multi-scale analysis reveals the dual role of in situ SEI as a "growth binder" at low current densities and an "orientation regulator" at high current densities for Zn deposits. As a consequence, symmetric Zn// Zn cells present record-breaking cumulative stability compared to previous reports (1300 h at 50 $mA cm^{-2}$; 400 h at 100 $mA cm^{-2}$). Demonstrating excellent reversibility, the Zn//PANI full batteries exhibit ultra stable cycling performance over 3000 cycles. Even under harsh conditions, Zn// PANI full cells have excellent cycling performance with high-mass loading condition. This work demonstrates a promising dual reaction strategy for the composition and structural design of SEI, not only advances the understanding of SEI formation in ZIBs but also opens a new avenue to design advanced SEIs for other emerging battery systems.

Supporting Information

Detailed experimental procedures, characterization analysis and electrochemical measurement. Including Figures S1–S33, and Tables S1–S3.

Acknowledgements

This work is supported by the Natural Science Foundation of China (Grant No. 22409194), the Energy Revolution S&T Program of Yulin Innovation Institute of Clean Energy, (Grant No. YICE E411060316), the Strategic Priority Research Program of the Chinese Academy of Sciences (Grant No. XDB0600000, XDB0600200), and the Postdoctoral Fellowship Program of CPSF (Grant No. GZB20230726).The authors are grateful for the technical support for Vacuum Interconnected Nanotech Workstation (Nano-X) from Suzhou Institute of Nano-Tech and Nano-Bionics, Chinese Academy of Sciences (SINANO). And the authors would like to thank Dr. Tong Liu for the help in FIB collection and Dr. Qing Zhang for conducting the XPS characterizations.

Conflict of Interest

The authors declare no conflict of interest.

Data Availability Statement

The data that support the findings of this study are available from the corresponding author upon reasonable request.

Keywords: Aqueous zinc-ion batteries 1 · solid-electrolyte interface 2 · electrolyte additive 3 · in situ construction 4 · electrostatic interaction 5

[1] M. Armand, J. Tarascon, *Nature* **2008**, *451*, 652–657.
[2] J. W. Choi, D. Aurbach, *Nat. Rev. Mater.* **2016**, *1*(4), 16013.
[3] C. Hu, L. Gong, Y. Xiao, Y. Yuan, N. M. Bedford, Z. Xia, L. Ma, T. Wu, Y. Lin, J. W. Connell, R. Shahbazian-Yassar, J. Lu, K. Amine, L. Dai, *Adv. Mater.* **2020**, *32*(16), 1907436.
[4] L. Qian, T. Or, Y. Zheng, M. Li, D. Karim, A. Cui, M. Ahmed, H. W. Park, Z. Zhang, Y. Deng, *Renewables* **2023**, *1*(2), 114–141.
[5] F. Wang, O. Borodin, T. Gao, X. Fan, W. Sun, F. Han, A. Faraone, J. A. Dura, K. Xu, C. Wang, *Nat. Mater.* **2018**, *17*, 543–549.
[6] F. Mo, G. Liang, Q. Meng, Z. Liu, H. Li, J. Fan, C. Zhi, *Energy Environ. Sci.* **2019**, *12*(2), 706–715.
[7] N. Wang, C. Sun, X. Liao, Y. Yuan, H. Cheng, Q. Sun, B. Wang, X. Pan, K. Zhao, Q. Xu, X. Lu, J. Lu, *Adv. Energy Mater.* **2020**, *10*(16), 2002293.
[8] F. Wang, J. Zhang, H. Lu, H. Zhu, Z. Chen, L. Wang, J. Yu, C. You, W. Li, J. Song, Z. Weng, C. Yang, Q.-H. Yang, *Nat. Commun.* **2023**, *14*(1), 4211.
[9] Y. Yin, X. Li, *Renewables* **2023**, 1–16.

[10] J. Hao, L. Yuan, C. Ye, D. Chao, K. Davey, Z. Guo, S. Z. Qiao, *Angew. Chem. Int. Ed.* **2021**, *60*(13), 7366–7375.
[11] M. Li, X. Wang, J. Hu, J. Zhu, C. Niu, H. Zhang, C. Li, B. Wu, C. Han, L. Mai, *Angew. Chem. Int. Ed.* **2023**, *62*(8), e202215552.
[12] X.-X. Zeng, S. Zhang, T. Long, Q.-Y. Zhao, H.-R. Wang, W. Ling, X.-W. Wu, A. Yu, Z. Chen, *Renewables* **2024**, 1–17.
[13] D. Yuan, J. Zhao, H. Ren, Y. Chen, R. Chua, E. T. J. Jie, Y. Cai, E. Edison, W. Manalastas Jr, M. W. Wong, *Angew. Chem. Int. Ed.* **2021**, *60*(13), 7213–7219.
[14] W. Xu, J. Li, X. Liao, L. Zhang, X. Zhang, C. Liu, K. Amine, K. Zhao, J. Lu, *J. Am. Chem. Soc.* **2023**, *145*(41), 22456–22465.
[15] D. Hoang, Y. Li, M. S. Jung, S. K. Sandstrom, A. M. Scida, H. Jiang, T. C. Gallagher, B. A. Pollard, R. Jensen, N.-C. Chiu, K. Stylianou, W. F. Stickle, P. A. Greaney, X. Ji, *Adv. Energy Mater.* **2023**, *13*(42), 2301712.
[16] J. Zhou, M. Xie, F. Wu, Y. Mei, Y. Hao, R. Huang, G. Wei, A. Liu, L. Li, R. Chen, *Adv. Mater.* **2021**, *33*(33), 2101649.
[17] X. Zhang, J. Li, D. Liu, M. Liu, T. Zhou, K. Qi, L. Shi, Y. Zhu, Y. Qian, *Energy Environ. Sci.* **2021**, *14*(5), 3120–3129.
[18] Y. Wang, T. Guo, J. Yin, Z. Tian, Y. Ma, Z. Liu, Y. Zhu, H. N. Alshareef, *Adv. Mater.* **2022**, *34*(4), 2106937.
[19] X. Wang, X. Li, H. Fan, L. Ma, *Nano-Micro Lett.* **2022**, *14*(1), 205.
[20] S. Bai, Z. Huang, G. Liang, R. Yang, D. Liu, W. Wen, X. Jin, C. Zhi, X. Wang, *Adv. Sci.* **2024**, *11*(4), 2304549.
[21] F. Ming, Y. Zhu, G. Huang, A.-H. Emwas, H. Liang, Y. Cui, H. N. Alshareef, *J. Am. Chem. Soc.* **2022**, *144*(16), 7160–7170.
[22] G. Liang, Z. Tang, B. Han, J. Zhu, A. Chen, Q. Li, Z. Chen, Z. Huang, X. Li, Q. Yang, *Adv. Mater.* **2023**, *35*(20), 2210051.
[23] Y. Zhu, J. Yin, X. Zheng, A.-H. Emwas, Y. Lei, O. F. Mohammed, Y. Cui, H. N. Alshareef, *Energy Environ. Sci.* **2021**, *14*(8), 4463–4473.
[24] L. Cao, D. Li, T. Pollard, T. Deng, B. Zhang, C. Yang, L. Chen, J. Vatamanu, E. Hu, M. J. Hourwitz, *Nat. Nanotechnol.* **2021**, *16*(8), 902–910.
[25] C. Li, A. Shyamsunder, A. G. Hoane, D. M. Long, C. Y. Kwok, P. G. Kotula, K. R. Zavadil, A. A. Gewirth, L. F. Nazar, *Joule* **2022**, *6*(5), 1103–1120.
[26] P. Albertus, S. Babinec, S. Litzelman, A. Newman, *Nat. Energy* **2018**, *3*(1), 16–21.
[27] L. Ma, M. A. Schroeder, O. Borodin, T. P. Pollard, M. S. Ding, C. Wang, K. Xu, *Nat. Energy* **2020**, *5*(10), 743–749.
[28] Y. Li, Z. Yu, J. Huang, Y. Wang, Y. Xia, *Angew. Chem. Int. Ed.* **2023**, *62*(47), e202309957.
[29] L. Yuan, J. Hao, C.-C. Kao, C. Wu, H.-K. Liu, S.-X. Dou, S.-Z. Qiao, *Energy Environ. Sci.* **2021**, *14*(11), 5669–5689.
[30] Q.-K. Zhang, X.-Q. Zhang, J. Wan, N. Yao, T.-L. Song, J. Xie, L.-P. Hou, M.-Y. Zhou, X. Chen, B.-Q. Li, *Nat. Energy* **2023**, *8*, 725–735.
[31] J. Wagner-Henke, D. Kuai, M. Gerasimov, F. Röder, P. B. Balbuena, U. Krewer, *Nat. Commun.* **2023**, *14*(1), 6823.
[32] J. Weng, W. Zhu, K. Yu, J. Luo, M. Chen, L. Li, Y. Zhuang, K. Xia, Z. Lu, Y. Hu, *Adv. Funct. Mater.* **2024**, 2316788.
[33] X. Zeng, J. Mao, J. Hao, J. Liu, S. Liu, Z. Wang, Y. Wang, S. Zhang, T. Zheng, J. Liu, *Adv. Mater.* **2021**, *33*(11), 2007416.
[34] Y. Liu, Y. An, L. Wu, J. Sun, F. Xiong, H. Tang, S. Chen, Y. Guo, L. Zhang, Q. An, *ACS Nano* **2022**, *17*(1), 552–560.
[35] T. Wang, Q. Xi, Y. Li, H. Fu, Y. Hua, E. G. Shankar, A. K. Kakarla, J. S. Yu, *Adv. Sci.* **2022**, *9*(18), 2200155.
[36] G. Liang, J. Zhu, B. Yan, Q. Li, A. Chen, Z. Chen, X. Wang, B. Xiong, J. Fan, J. Xu, *Energy Environ. Sci.* **2022**, *15*(3), 1086–1096.
[37] Y. Wang, B. Liang, J. Zhu, G. Li, Q. Li, R. Ye, J. Fan, C. Zhi, *Angew. Chem. Int. Ed.* **2023**, *62*(23), e202302583.
[38] Z. Bie, Q. Yang, X. Cai, Z. Chen, Z. Jiao, J. Zhu, Z. Li, J. Liu, W. Song, C. Zhi, *Adv. Energy Mater.* **2022**, *12*(44), 2202683.
[39] Y. Lyu, J. A. Yuwono, P. Wang, Y. Wang, F. Yang, S. Liu, S. Zhang, B. Wang, K. Davey, J. Mao, *Angew. Chem. Int. Ed.* **2023**, *62*(21), e202303011.
[40] D. Han, C. Cui, K. Zhang, Z. Wang, J. Gao, Y. Guo, Z. Zhang, S. Wu, L. Yin, Z. Weng, *Nat. Sustain.* **2022**, *5*(3), 205–213.
[41] Z. Shen, J. Mao, G. Yu, W. Zhang, S. Mao, W. Zhong, H. Cheng, J. Guo, J. Zhang, Y. Lu, *Angew. Chem. Int. Ed.* **2023**, *135*(11), e202218452.
[42] M. Peng, X. Tang, K. Xiao, T. Hu, K. Yuan, Y. Chen, *Angew. Chem. Int. Ed.* **2023**, *135*(27), e202302701.
[43] Y. Lin, Z. Mai, H. Liang, Y. Li, G. Yang, C. Wang, *Energy Environ. Sci.* **2023**, *16*(2), 687–697.
[44] P. Wang, S. Liang, C. Chen, X. Xie, J. Chen, Z. Liu, Y. Tang, B. Lu, J. Zhou, *Adv. Mater.* **2022**, *34*(33), 2202733.
[45] Y. Okazaki, T. Taniuchi, G. Mogami, N. Matubayasi, M. Suzuki, *J. Phys. Chem. A* **2014**, *118*(16), 2922–2930.
[46] Y. Ma, Q. Zhang, L. Liu, Y. Li, H. Li, Z. Yan, J. Chen, *Natl. Sci. Rev.* **2022**, *9*(10), nwac051.
[47] F. Sterpone, G. Stirnemann, J. T. Hynes, D. Laage, *J. Phys. Chem. B* **2010**, *114*(5), 2083–2089.
[48] H. Li, Y. Ren, Y. Zhu, J. Tian, X. Sun, C. Sheng, P. He, S. Guo, H. Zhou *Angew. Chem. Int. Ed.* **2023**, *62*(41), e202310143.
[49] L. Zhou, F. Yang, S. Zeng, X. Gao, X. Liu, X. Cao, P. Yu, X. Lu, *Adv. Funct. Mater.* **2022**, *32*(15), 2110829.
[50] X. Wang, K. Feng, B. Sang, G. Li, Z. Zhang, G. Zhou, B. Xi, X. An, S. Xiong, *Adv. Energy Mater.* **2023**, *13*(36), 2301670.
[51] W. Chen, S. Guo, L. Qin, L. Li, X. Cao, J. Zhou, Z. Luo, G. Fang, S. Liang *Adv. Funct. Mater.* **2022**, *32*(20), 2112609.
[52] H. Wang, W. Ye, B. Yin, K. Wang, M. S. Riaz, B. B. Xie, Y. Zhong, Y. Hu, *Angew. Chem. Int. Ed.* **2023**, *62*(10), e202218872.
[53] K. Ouyang, D. Ma, N. Zhao, Y. Wang, M. Yang, H. Mi, L. Sun, C. He, P. Zhang, *Adv. Funct. Mater.* **2022**, *32*(7), 2109749.
[54] D. Li, Y. Tang, S. Liang, B. Lu, G. Chen, J. Zhou, *Energy Environ. Sci.* **2023**, *16*, 3381–3390.
[55] X. Wang, Y. Ying, X. Li, S. Chen, G. Gao, H. Huang, L. Ma, *Energy Environ. Sci.* **2023**, *16*, 4572–4583.
[56] T. Yan, S. Liu, J. Li, M. Tao, J. Liang, L. Du, Z. Cui, H. Song, *ACS Nano* **2024**, *18*, 3752–3762.
[57] K. Wang, T. Qiu, L. Lin, H. Zhan, X.-X. Liu, X. Sun, *ACS Energy Lett.* **2024**, *9*, 1000–1007.
[58] L. Zhang, L. Miao, W. Xin, H. Peng, Z. Yan, Z. Zhu, *Energy Storage Mater.* **2022**, *44*, 408–415.
[59] J. Li, S. Zhou, Y. Chen, X. Meng, A. Azizi, Q. He, H. Li, L. Chen, C. Han, A. Pan, *Adv. Funct. Mater.* **2023**, *33*(52), 2307201.
[60] J. Zhang, W. Huang, L. Li, C. Chang, K. Yang, L. Gao, X. Pu, *Adv. Mater.* **2023**, *35*(21), 2300073.
[61] Z. Cai, J. Wang, Z. Lu, R. Zhan, Y. Ou, L. Wang, M. Dahbi, J. Alami, J. Lu, K. Amine, Y. Sun, *Angew. Chem. Int. Ed.* **2022**, *61*(14), e202116560.
[62] S. Zhai, W. Song, K. Jiang, X. Tan, W. Zhang, Y. Yang, W. Chen, N. Chen, H. Zeng, H. Li, Z. Li, *Energy Environ. Sci.* **2023**, *16*(11), 5479–5489.

Manuscript received: April 25, 2024
Accepted manuscript online: July 12, 2024
Version of record online: September 3, 2024

Correction done on 16.09.2024: Supporting Information has been uploaded to this article.